Chinese Physics Letters

PAPER

Orbital-Ordering Driven Simultaneous Tunability of Magnetism and Electric Polarization in Strained Monolayer VCl_3

To cite this article: Deping Guo *et al* 2024 *Chinese Phys. Lett.* **41** 047501

Orbital-Ordering Driven Simultaneous Tunability of Magnetism and Electric Polarization in Strained Monolayer VCl_3

Deping Guo(郭的坪)[1,2†], Cong Wang(王聪)[1,2†], Lvjin Wang(王侣锦)[1,2], Yunhao Lu(陆赟豪)[3], Hua Wu(吴骅)[4], Yanning Zhang(张妍宁)[5], and Wei Ji(季威)[1,2,5*]

[1]*Beijing Key Laboratory of Optoelectronic Functional Materials & Micro-Nano Devices, Department of Physics, Renmin University of China, Beijing 100872, China*

[2] *Key Laboratory of Quantum State Construction and Manipulation (Ministry of Education), Renmin University of China, Beijing 100872, China*

[3]*Zhejiang Province Key Laboratory of Quantum Technology and Device, State Key Laboratory of Silicon Materials, Department of Physics, Zhejiang University, Hangzhou 310027, China*

[4]*Laboratory for Computational Physical Sciences (MOE), State Key Laboratory of Surface Physics, and Department of Physics, Fudan University, Shanghai 200433, China*

[5]*Institute of Fundamental and Frontier Sciences, University of Electronic Science and Technology of China, Chengdu 610054, China*

(Received 30 January 2024; accepted manuscript online 21 March 2024)

Two-dimensional (2D) van der Waals magnetic materials have promising and versatile electronic and magnetic properties in the 2D limit, indicating a considerable potential to advance spintronic applications. Theoretical predictions thus far have not ascertained whether monolayer VCl_3 is a ferromagnetic (FM) or anti-FM monolayer; this also remains to be experimentally verified. We theoretically investigate the influence of potential factors, including C_3 symmetry breaking, orbital ordering, epitaxial strain, and charge doping, on the magnetic ground state. Utilizing first-principles calculations, we predict a collinear type-Ⅲ FM ground state in monolayer VCl_3 with a broken C_3 symmetry, wherein only the former two of three t_{2g} orbitals (a_{1g}, e^{π}_{g2} and e^{π}_{g1}) are occupied. The atomic layer thickness and bond angles of monolayer VCl_3 undergo abrupt changes driven by an orbital ordering switch, resulting in concomitant structural and magnetic phase transitions. Introducing doping to the underlying Cl atoms of monolayer VCl_3 without C_3 symmetry simultaneously induces in- and out-of-plane polarizations. This can achieve a multiferroic phase transition if combined with the discovered adjustments of magnetic ground state and polarization magnitude under strain. The establishment of an orbital-ordering driven regulatory mechanism can facilitate deeper exploration and comprehension of magnetic properties of strongly correlated systems in monolayer VCl_3.

DOI: 10.1088/0256-307X/41/4/047501

Two-dimensional (2D) magnetic materials have recently garnered substantial attention because of their promising applications in spintronics,[1–4] including magnetic logical devices,[5–7] storage,[8] and sensors.[9] The discovery of the first monolayer ferromagnetic (FM) CrI_3 in 2017[7] has paved the way for continuous experimental confirmations of monolayer magnets, such as Fe_3GeTe_2,[10] CrOCl,[11] CrSBr,[12,13] $CrTe_2$,[14] and $CrSe_2$,[15] substantially augmenting the diversity of available 2D magnets. In addition to various strategies for tuning interlayer magnetism,[16–19] intralayer magnetism within a monolayer magnet can be modified through approaches such as breaking geometric symmetry,[20] applying in-plane (IP) strain,[21] and introducing electric doping.[22] Moreover, orbital ordering in open-shell magnetic cations can add a new dimension to the tunability of intralayer magnetism.[23]

The V cation in 2D vanadium trihalides VX_3 ($X = $ Cl, Br, or I) is an open-shell cation with a valence of 3+, leaving two $3d$ electrons to fill three t_{2g} orbitals. These originally degenerate triplet t_{2g} orbitals split into a singlet (a_{1g}) and doublet (e^{π}_{g}) owing to the presence of a triangular crystal field.[23–25] Despite variations in their orbital orderings,[23,24] both VI_3 and VBr_3 monolayers have been identified as FM insulators. However, the magnetic ground state of VCl_3 remains indeterminate between those of an FM Dirac semimetal[26,27] and a zigzag (ZZ) anti-FM (AFM) semiconductor.[28] Hence, subtle tunability among different magnetic configurations of monolayer VCl_3 may exist, implying a potential FM/AFM transition under external perturbations. Moreover, a magnetic transition driven by the alteration of orbital orderings is often associated with structural symmetry variations,[29,30] such as the elimination or introduction of structural inversion

†These authors contributed equally to this work.

*Corresponding author. Email: wji@ruc.edu.cn

or C_3 rotational symmetry. This may lead to simultaneous variations in electric polarization and magnetization.

In this work, we theoretically explored the tunability of the magnetic and electric polarization properties in monolayer VCl_3 subjected to uniaxial strain and charge doping, with orbital ordering serving as the driving mechanism. Our analysis encompassed 18 configurations from three structural classifications and six magnetic orders for the VCl_3 monolayer. An FM semiconducting state characterized by the absence of IP C_3 rotational symmetry is the global ground state for the strain-free monolayer VCl_3. For simplicity, we adopted the FM configuration with C_3 symmetry as the strain-free reference configuration. Then, we modulated the magnetic properties of monolayer VCl_3 under uniaxial epitaxial x-strain, which is correlated with geometric structures and orbital ordering. We further examined the electric polarization properties of strained monolayer VCl_3 under electron doping, which can induce out-of-plane (OOP) and IP electric polarization. In addition, uniaxial y-axis strain and biaxial epitaxial strains were considered.

We performed density functional theory calculations using the generalized gradient approximation for the exchange-correlation potential,[31] projector augmented wave method,[32,33] and a plane-wave basis set, as implemented in Vienna *ab initio* simulation package (VASP).[34,35] In addition, dispersion correction was achieved using Grimme's D3 form PBE-D3.[31,36] Moreover, to account for on-site Coulomb interactions within the V $3d$ orbitals, the DFT + U method[37] was applied with an effective U value of 3.0 eV, which was similar to that used in other studies.[20,26,38] The cut-off kinetic energy for the plane-wave basis set was set to 700 eV in both structural relaxations and total energy calculations. All the geometric structures were fully relaxed until the residual force per atom was less than 0.005 eV/Å. A $2\times\sqrt{3}\times1$ rectangular supercell was used to compare the total energies of different magnetic configurations, ensuring energy comparisons under the same conditions. A $7\times9\times1$ k-mesh was adopted to sample the Brillouin zone of the $2\times\sqrt{3}\times1$ supercell. A vacuum layer over 15 Å in thickness was adopted to eliminate interactions among image slabs. Uniaxial epitaxial strains along the $x(y)$ axis were applied to the FM structure of monolayer VCl_3 (with C_3 symmetry) by varying the lattice constant along the $x(y)$ axis while maintaining it along the $y(x)$ axis. Biaxial strains were also implemented by assigning certain sets of x and y lattice constants to the monolayer. Charge doping was achieved through the ionic potential method,[39] which ensured the neutrality of the supercell and confined exceeding electrons around the doped atoms. The Cl $2s$ orbital core potential was modified[40] to accumulate the doped electrons on Cl atoms in the bottom sublayer. The electric polarizations were derived using the Berry phase method.[41] The thickness of the atomic layer (h) was quantified by identifying the highest and lowest positions of the Cl atoms in monolayer VCl_3. As the θ_1 values were identical for different octahedral under uniaxial strain along the x axis, only one θ_1 value was evaluated under different strains.

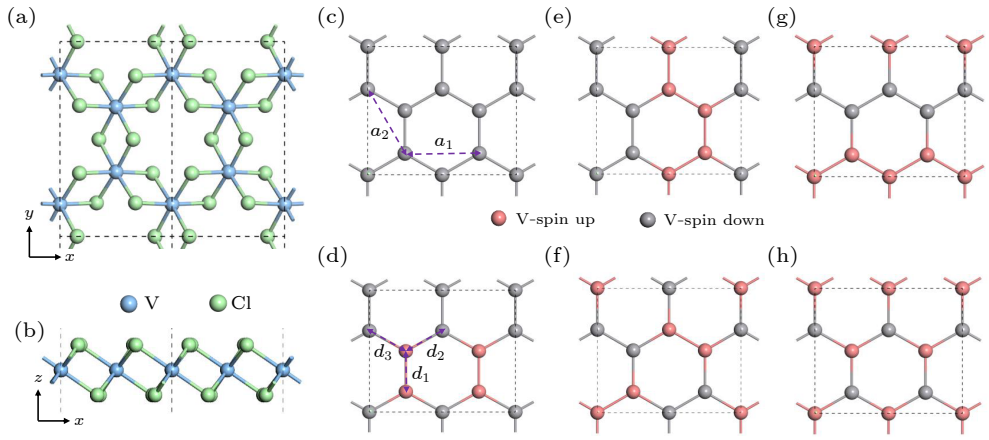

Fig. 1. (a) Top and (b) side views of fully relaxed geometric structure of monolayer VCl_3 in $1\times\sqrt{3}\times1$ supercell. The light blue and green balls represent V and Cl atoms, respectively. Illustrations of (c) FM, (d) bi-stripe-AFM state, (e) armchair-AFM state, (f) bi-Néel-AFM state, (g) ZZ-AFM state, and (h) Néel-AFM state. The gray and pink balls represent up and down majority spins of V atoms, respectively. Variables d_1, d_2, and d_3 (a_1 and a_2) denote the nearest (second-nearest) neighbor V–V distances along three (two) directions.

Freestanding monolayer VCl_3 exhibited geometric similarities with monolayer CrX_3 (X = Cl, Br, or I), where M–Cl (M = V or Cr) octahedra shared common edges and coalesced into a hexagonal monolayer that displayed IP C_3 rotational symmetry. Figures 1(a) and 1(b) show the top and side views of the monolayer VCl_3 atomic structure within two rectangular $1\times\sqrt{3}$ supercells. Figures 1(c)–1(h) show the six magnetic orders considered for each structural category in rectangular $2\times\sqrt{3}$ supercells to ascertain the magnetic ground state. The three nearest-neighbor V–V atomic distances, denoted as d_1–d_3 [see Fig. 1(d)], divide the fully relaxed geometric structures into three categories,

as listed in Table 1. While the C_3 rotational symmetry is nearly preserved in type-I structures, the symmetry breaks in both type-Ⅱ and type-Ⅲ structures. The critical distinction between type-Ⅱ and type-Ⅲ structures lies in whether d_1 is smaller (type-Ⅱ) or larger (type-Ⅲ) than d_2 and d_3.

Among all the type-I configurations with (nearly) preserved C_3 rotational symmetry, the FM state is the energetically favored configuration, exhibiting lattice constant $a = 6.092$ Å, equivalent to $d_1 = d_2 = d_3 = 3.517$ Å. The breakdown of the C_3 symmetry results in a lower energy state for most magnetic configurations within the type-Ⅱ and Ⅲ categories, as indicated by their reduced total energies compared with their type-I counterparts (see Table 1). Only three (type-Ⅱ) and four (type-Ⅲ) magnetic configurations are listed in Table 1 because not all magnetic orders could be obtained in structures with broken C_3 symmetry. Remarkably, the global ground state is type-Ⅲ FM characterized by lattice constants $a_1 = 6.156$ Å, $a_2 = 6.105$ Å, $d_1 = 3.543$ Å, and $d_2 = d_3 = 3.530$ Å. The second most stable configuration is type-Ⅲ ZZ AFM, which is 2.6 meV/VCl_3 less stable than type-Ⅲ FM. The stability of monolayer VCl_3 is substantially influenced by the preservation of C_3 symmetry. Despite minor numerical differences in V–V distances between the type-I and type-Ⅲ FM configurations, a large energy difference of 16.6 meV/VCl_3 is observed. Given the nearly identical atomic structures and consistent FM order, this difference implies that the orbital ordering most likely plays a paramount role ascribed to the open-shell V cation in monolayer VCl_3.

Table 1. Structural parameters and total energies of six magnetic configurations. Here a_1 and a_2 are the distances between the next-nearest-neighbor V atoms, and d_1–d_3 are the distances between the nearest-neighbor V atoms [marked in Figs. 1(c) and 1(d)].

	Magnetic configuration	a_1 (Å)	a_2 (Å)	d_1 (Å)	d_2 (Å)	d_3 (Å)	Energy (meV/VCl_3)	C_3 symmetry
Type-I	FM	6.092	6.092	3.517	3.517	3.517	16.6	Yes (Nearly)
	ZZ-AFM	6.086	6.089	3.510	3.517	3.517	18.8	
	AC-AFM	6.089	6.090	3.517	3.513	3.516	19.0	
	BS-AFM	6.089	6.088	3.516	3.514	3.514	22.4	
	BN-AFM	6.087	6.088	3.515	3.515	3.515	22.3	
	Néel AFM	6.067	6.067	3.503	3.503	3.503	518.8	
Type-Ⅱ	FM	6.155	6.106	3.526	3.539	3.539	18.1	No ($d_1 < d_2$, d_3)
	BN-AFM	6.099	6.117	3.515	3.532	3.536	5.7	
	Néel AFM	6.098	6.113	3.519	3.530	3.530	7.3	
Type-Ⅲ	FM	6.156	6.105	3.543	3.530	3.530	0	No ($d_1 > d_2$, d_3)
	ZZ-AFM	6.163	6.110	3.555	3.529	3.529	2.6	
	BS-AFM	6.121	6.100	3.534	3.522	3.522	5.1	
	Néel AFM	6.127	6.102	3.536	3.524	3.524	6.8	

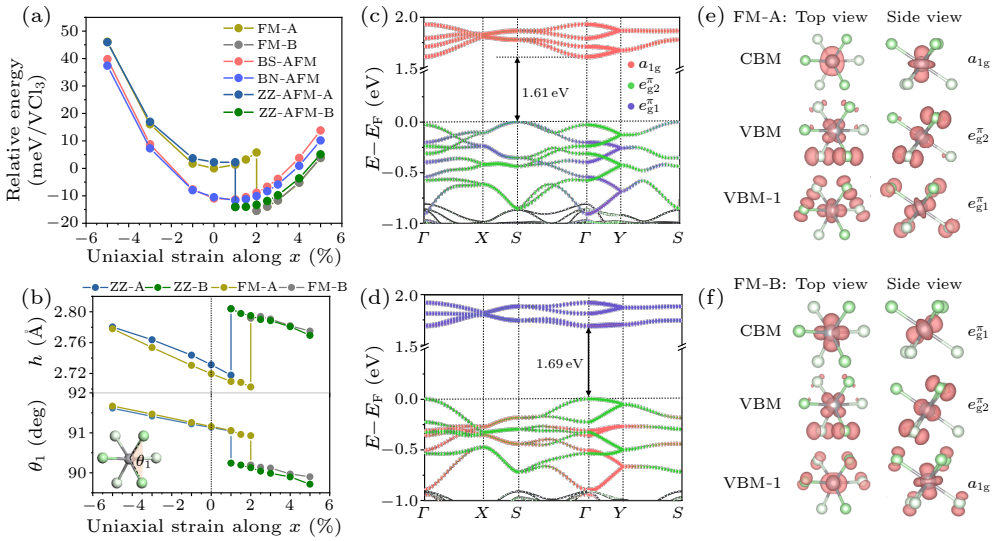

Fig. 2. (a) Energy–strain relation under uniaxial strain along the x axis in FM state (gray and olive) as well as bi-stripe-AFM state (red), bi-Néel-AFM state (royal blue), and ZZ-AFM (green and dark blue) state. The energy of the strain-free type-I FM configuration is chosen as the zero-energy reference. (b) Variations in layer thickness h and Cl–V–Cl angle θ_1 under uniaxial x-axis strain in FM and ZZ-AFM orders. Orbital-resolved band structures of (c) FM-A and (d) FM-B under 2% uniaxial x-axis strain. Plots of wavefunction norms for conduction band minimum (CBM), valence band maximum (VBM), and VBM-1 (i.e., band below VBM) state at the Γ point of (e) FM-A and (f) FM-B under 2% x-axis strain. The isosurface values are set to $2 \times 10^{-3}\, e/\text{Bohr}^3$.

Uniaxial epitaxial strain was applied to the fully relaxed $2 \times \sqrt{3} \times 1$ type-I FM supercell along the x or y axis, in which three magnetic transitions were observed. Figure 2(a) shows the total energies of the bi-stripe (BS)-AFM, bi-Néel (BN)-AFM, ZZ-AFM, and FM orders under uniaxial x-axis strain in the range of $\pm 5\%$. We employed the strain-free type-I FM configuration as the reference lattice (0.0%) to evaluate the strain effects. Under 0% strain lattice, the BN-AFM (royal blue dots) and BS-AFM (red dots) configurations, which lack C_3 structural symmetry, are more stable than the FM configuration by 10.5 and 11.0 meV/VCl_3, respectively [Fig. 2(a)]. The BN-AFM order becomes the magnetic ground state for x-axis compressive strain exceeding 1%. For tensile strains, the energy of the ZZ-AFM order drops below those of the BN- and BS-AFM orders at 1% x-axis tensile strain, becoming the global ground state. Further increasing the tensile strain to 2% abruptly reduces the energy of the FM order, and the ground state shifts to another FM state. The FM state maintains its superior stability up to at least 5% x-axis strain, indicating that the magnetic ground state transforms from BN-AFM to ZZ-AFM and then to FM under epitaxial tensile strain along the x axis.

The abrupt variation in energies indicate the existence of two categories of ZZ-AFM (FM) configurations, which were characterized by orbital ordering, as detailed below. The ZZ-AFM (FM) state before the abrupt variation is termed as set A comprising the ZZ-AFM-A and FM-A states, whereas set B comprises the ZZ-AFM-B and FM-B states after that abrupt variation. The ZZ-AFM-A/ZZ-AFM-B transition is indicative of an abrupt increase of approximately 0.1 Å in the atomic layer thickness h and decrease in angle θ_1 of approximately 1° under 1% tensile strain [Fig. 2(b)], with a corresponding negative Poisson's ratio (−5.9) during the transition. This anomalous structural change is similarly observed in the FM-A/FM-B transition at 2% tensile x-axis strain. Moreover, this structural alternation coincides with a transition from an indirect [1.61 eV, FM-A, Fig. 2(c)] to a direct [1.69 eV, FM-B, Fig. 2(d)] bandgap. This abrupt change in both the bandgap value and band dispersion suggests a substantial electronic structure alternation, signaling a rearrangement in the ordering of the t_{2g} orbitals. To examine the orbital orderings, we projected the band structures onto the one a_{1g} and two e_g^π orbitals [Figs. 2(c) and 2(d)]. The projections demonstrate that these two FM states possess different orbital orderings, where a_{1g} (red) and e_{g1}^π (violet) are unoccupied in FM-A and FM-B, respectively. The wavefunction norms of these states plotted around the bandgap at the Γ point are shown in Figs. 2(e) and 2(f). Their shapes and energy levels corroborate the orbital orderings inferred from the band structure projections [Figs. 2(c) and 2(d)].

Then, we elucidated the mechanism underlying the changes in orbital ordering induced by x-axis strain. Upon stretching along the x axis, both the layer thickness (h) and Cl–V–Cl bond angle (θ_1) initially decrease [Fig. 2(b)], prompting the V–Cl bonds to approach closer to the plane of the V e_{g1}^π orbital. This gradual reduction in the octahedral space promotes the wavefunction to overlap between the V–Cl σ-bonding state and e_{g1}^π orbital. This strengthened non-bonding wavefunction overlap enhances the Pauli and Coulomb repulsions between the V–Cl σ-bonding state and e_{g1}^π orbital, rendering the e_{g1}^π orbital less stable upon lattice stretching. A transition characterized by an intersection of the orbital energies occurs at approximately 2% x-axis strain, resulting in the e_{g1}^π orbital becoming unoccupied as the progressively intensified repulsion elevates it above the Fermi level. Thus, the initially unoccupied a_{1g} orbital in FM-A [Fig. 2(e)] reaches a lower energy state and becomes occupied in FM-B [Fig. 2(f)] owing to the abrupt increase in the atomic layer thickness. The increased thickness (h) in FM-B provides additional space within the V–Cl octahedron, drastically reducing the repulsion between the a_{1g} orbital and V–Cl bonding state, thereby reducing the a_{1g} orbital energy and rendering it occupied. These results indicate that strain-induced alterations in the electronic structure and magnetism of monolayer VCl_3 are governed by changes in orbital orderings. Therefore, a new dimension for tuning the electronic and magnetic properties of VCl_3 becomes available through epitaxial strain; tuning can also be achieved by charge doping, as discussed in the following.

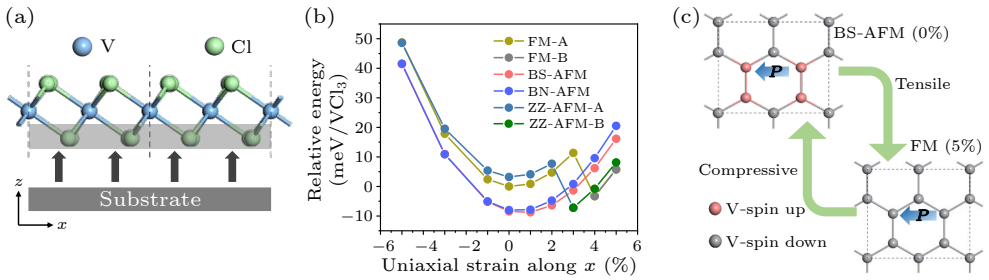

Fig. 3. (a) Schematic of epitaxial strain and doping between substrate and monolayer VCl_3. (b) Energy–strain relation under uniaxial strain along x axis and doping with 0.01 e/Cl of bottom layer in FM as well as BS-AFM, BN-AFM, and ZZ-AFM states. The energy reference is consistent with that adopted in Fig. 2, namely, the total energy of the strain-free type-I FM configuration. (c) Transition between BS-AFM and FM states under x-axis strain and doping.

When a 2D material epitaxially grows on a substrate, charge transfers often coexist at the interface with epitaxial strain. To model this charge doping effect, we introduced 0.01 e/Cl doping to the bottom Cl atoms of monolayer VCl_3 and explored the magnetic properties under uniaxial x-axis strain. As shown in Fig. 3(b), this uniform doping does not change the magnetic ground state of the strain-free lattice. The BS-AFM order maintains its superior stability under 0% uniaxial x-axis strain. As the x-axis strain increases to 3%, the ZZ-AFM-B order becomes the magnetic ground state [Fig. 3(b)]. A ZZ-AFM-B to FM-B magnetic transition occurs when the x-axis tensile strain increases to 4%. The results indicate that charge doping does not qualitatively change the sequence of strain induced magnetic transitions, but shifts the critical strains to higher values.

Charge doping from the substrate has been reported to break the inversion symmetry in monolayer CrI_2, leading to IP polarization.[42] In this study, charge doping on the interfacial Cl layer of type-I FM breaks the structural inversion symmetry, resulting in an OOP electric polarization. A 0.01 e/Cl-doped type-I FM monolayer VCl_3 retaining C_3 symmetry exhibits OOP electric polarization of 0.03 $\mu C/cm^2$; this value highly depends on the doping level. For instance, a higher doping level increases the electric polarization. In particular, OOP polarization increases to 0.12 $\mu C/cm^2$ in a 0.10 e/Cl-doped type-I FM monolayer.

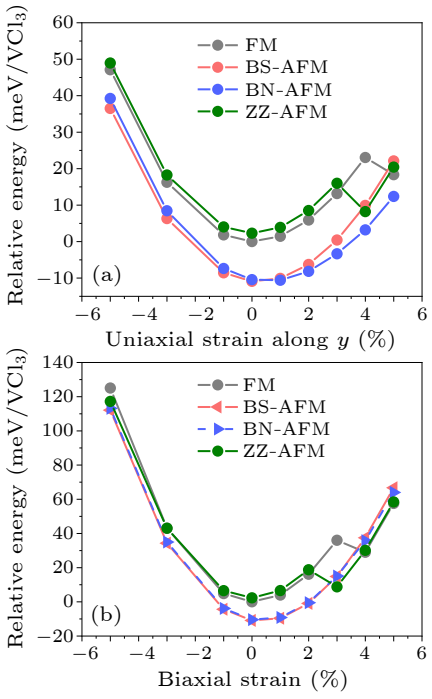

Fig. 4. (a) Energy–strain relationship under uniaxial strain along y axis in FM (gray) as well as BS-AFM (red), BN-AFM (blue), and ZZ-AFM (green) states. (b) Energy–strain relationship under biaxial strain in FM as well as BS-AFM, BN-AFM, and ZZ-AFM states. The energy reference is consistent with that adopted in Figs. 2 and 3, namely, the total energy of the strain-free type-I FM configuration.

When the C_3 symmetry of monolayer VCl_3 is compromised (e.g., in the type-Ⅲ FM configuration), the inversion symmetry is retained in the absence of charge doping. If the inversion symmetry is previously compromised in monolayer VCl_3 by, for example, charge doping, the breakdown of IP C_3 rotational symmetry additionally introduces an IP electric polarization. For 0.01 e/Cl-doped BS-AFM monolayer VCl_3 lacking C_3 symmetry, an IP polarization of 0.012 $\mu C/cm^2$ appears along the x axis in addition to an OOP polarization of 0.009 $\mu C/cm^2$. In addition to inducing a magnetic phase transition, an increased strain typically increases the polarization value. For instance, the magnetic ground state transitions to the FM-B configuration under 5% uniaxial x-axis strain, and the IP polarization along the x-axis increased to 0.016 $\mu C/cm^2$ [Fig. 3(c)]. Although these polarization values are an order of magnitude smaller than those reported for 2D ferroelectricity,[43,44] the breakdown of C_3 symmetry offers an additional route to generate IP electric polarization in doped magnetic monolayer VCl_3. In essence, the x-axis strain leads to a BS-AFM to FM transition through orbital ordering accompanied by an increase in IP electric polarization in electron-doped monolayer VCl_3, as shown in Fig. 3(c). In other words, such strain evokes concurrent magnetic and electric polarization changes at the transition.

In addition to uniaxial x-axis strain, we have also considered uniaxial y-strains and biaxial epitaxial strains, observing orbital ordering driven transitions among different magnetic orders under strains up to ±5%. For the uniaxial y-axis strain [Fig. 4(a)], a BS-AFM to BN-AFM transition is observed for monolayer VCl_3. The BS-AFM configuration retains its superior stability from −5% to 1%, and the BN-AFM configuration emerges as the ground state for tensile strains exceeding 1%. For the biaxial strains, the BS- and BN-AFM configurations appear to be nearly degenerate within a strain range from −5% to 5% [Fig. 4(b)]. At a biaxial tensile strain of 3%, an orbital-ordering-driven magnetic transition is observed from the BS (BN)-AFM [blue (red)] to the ZZ-AFM configuration (green), resembling the uniaxial x-axis strain case shown in Fig. 2(a). These results reinforce the observed robustness of orbital-ordering driven changes in magnetism.

In summary, we theoretically investigated the magnetic and electric polarization properties of monolayer VCl_3 under the influence of uniaxial and biaxial epitaxial strains. The application of epitaxial x-axis strain distorted the shape of the V–Cl_6 octahedron, affecting the arrangement in energy levels among two e_g^{π} and one a_{1g} orbitals of the V cation. This modification in orbital ordering precipitated two representative magnetic transitions from the BS-AFM to the ZZ-AFM and subsequently to the FM order under tensile x-axis strain. Comparable transitions were also observed in the monolayer subjected to biaxial strains. Induced charge doping applied to the bottom layer Cl atoms compromised the structural inversion symmetry of the monolayer, thereby generating an OOP electric polarization. Furthermore, the additional breakdown of C_3

rotational symmetry added an IP component to electric polarization. The magnitude of electric polarization varied across different magnetic orders, establishing a relationship between magnetism and electric polarization in monolayer VCl_3. Our results suggest that strain-induced rearrangement in orbital ordering offers a novel route to select specific magnetic or electric polarization states in strategically strained open-shell monolayer VCl_3. This strategy may be applicable to other open-shell 2D magnets. The exploration of the roles of orbital ordering in modulating the magnetic, optical, and electric properties of open-shell 2D magnets remains an open field, necessitating further theoretical and experimental investigations.

Acknowledgements. We thank Dr. Junwei Liu at Hong Kong University of Science and Technology for the enlightening discussions. This work was supported by the National Key Research and Development Program of China (Grant Nos. 2018YFE0202700 and 2023YFA1406500), the National Natural Science Foundation of China (Grant Nos. 11974422 and 12104504), the Strategic Priority Research Program of the Chinese Academy of Sciences (Grant No. XDB30000000), Fundamental Research Funds for the Central Universities, and Research Funds of Renmin University, China (Grant No. 22XNKJ30). D.P.G. was supported by the Outstanding Innovative Talents Cultivation Funded Programs 2023 of Renmin University, China. The calculations for this study were performed at the Physics Lab of High-Performance Computing of Renmin University, China (PCC@RUC).

References

[1] Mak K F, Shan J, and Ralph D C 2019 *Natl. Rev. Phys.* **1** 646
[2] Gibertini M, Koperski M, Morpurgo A F, and Novoselov K S 2019 *Nat. Nanotechnol.* **14** 408
[3] Li H, Ruan S C, and Zeng Y J 2019 *Adv. Mater.* **31** 1900065
[4] Qi Y P, Sadi M A, Hu D, Zheng M, Wu Z P, Jiang Y C, and Chen Y P 2023 *Adv. Mater.* **35** 2205714
[5] Xu Z M, Li Y, Xu Y, and Duan W H 2020 *Chin. Sci. Bull.* **66** 535
[6] Zhang S Q, Xu R Z, Luo N N, and Zou X L 2021 *Nanoscale* **13** 1398
[7] Thiel L, Wang Z, Tschudin M A, Rohner D, Gutiérrez-Lezama I, Ubrig N, Gibertini M, Giannini E, Morpurgo A F, and Maletinsky P 2019 *Science* **364** 973
[8] Soumyanarayanan A, Reyren N, Fert A, and Panagopoulos C 2016 *Nature* **539** 509
[9] Fang Y M, Wu S Q, Zhu Z Z, and Guo G Y 2018 *Phys. Rev. B* **98** 125416
[10] Deng Y J, Yu Y J, Song Y C, Zhang J Z, Wang N Z, Sun Z Y, Yi Y F, Wu Y Z, Wu S W, Zhu J Y, Wang J, Chen X H, and Zhang Y B 2018 *Nature* **563** 94
[11] Miao N H, Xu B, Zhu L G, Zhou J, and Sun Z M 2018 *J. Am. Chem. Soc.* **140** 2417
[12] Lee K, Dismukes A H, Telford E J, Wiscons R A, Wang J, Xu X, Nuckolls C, Dean C R, Roy X, and Zhu X 2021 *Nano Lett.* **21** 3511
[13] Telford E J, Dismukes A H, Lee K, Cheng M, Wieteska A, Bartholomew A K, Chen Y S, Xu X, Pasupathy A N, Zhu X, Dean C R, and Roy X 2020 *Adv. Mater.* **32** 2003240
[14] Zhang X Q, Lu Q S, Liu W Q, Niu W, Sun J B, Cook J, Vaninger M, Miceli P F, Singh D J, Lian S W, Chang T R, He X, Du J, He L, Zhang R, Bian G, and Xu Y B 2021 *Nat. Commun.* **12** 2492
[15] Li B, Wan Z, Wang C, Chen P, Huang B W, Cheng X, Qian Q, Li J, Zhang Z, Sun G, Zhao B, Ma H, Wu R, Wei Z, Liu Y, Liao L, Ye Y, Huang Y, Xu X, Duan X D, Ji W, and Duan X F 2021 *Nat. Mater.* **20** 818
[16] Jiang P H, Wang C, Chen D C, Zhong Z C, Yuan Z, Lu Z Y, and Ji W 2019 *Phys. Rev. B* **99** 144401
[17] Huang B V, Clark G, Klein D R, MacNeill D, Navarro-Moratalla E, Seyler K L, Wilson N, McGuire M A, Cobden D H, Xiao D, Yao W, Jarillo-Herrero P, and Xu X 2018 *Nat Nanotechnol* **13** 544
[18] Wang C, Zhou X Y, Pan Y H, Qiao J S, Kong X H, Kaun C C, and Ji W 2018 *Phys. Rev. B* **97** 245409
[19] Wu L L, Zhou L W, Zhou X Y, Wang C, and Ji W 2022 *Phys. Rev. B* **106** L081401
[20] Huang C X, Wu F, Yu S L, Jena P, and Kan E J 2020 *Phys. Chem. Chem. Phys.* **22** 512
[21] Ma Y D, Dai Y, Guo M, Niu C W, Zhu Y, and Huang B 2012 *ACS Nano* **6** 1695
[22] Jiang S W, Li L Z, Wang Z F, Mak K F, and Shan J 2018 *Nat. Nanotechnol.* **13** 549
[23] Yang K, Fan F R, Wang H B, Khomskii D I, and Wu H 2020 *Phys. Rev. B* **101** 100402
[24] Liu L, Yang K, Wang G Y, and Wu H 2020 *J. Mater. Chem. C* **8** 14782
[25] Nguyen T P T, Yamauchi K, Oguchi T, Amoroso D, and Picozzi S 2021 *Phys. Rev. B* **104** 014414
[26] He J J, Ma S Y, Lyu P, and Nachtigall P 2016 *J. Mater. Chem. C* **4** 2518
[27] Zhou Y G, Lu H F, Zu X T, and Gao F 2016 *Sci. Rep.* **6** 19407
[28] Zhao S, Wan W, Ge Y, and Liu Y 2021 *Ann. Phys. (Berlin)* **533** 2100064
[29] Fiebig M, Lottermoser T, Meier D, and Trassin M 2016 *Natl. Rev. Mater.* **1** 16046
[30] Xu M L, Huang C X, Li Y W, Liu S Y, Zhong X, Jena P, Kan E, and Wang Y C 2020 *Phys. Rev. Lett.* **124** 067602
[31] Perdew J P, Burke K, and Ernzerhof M 1996 *Phys. Rev. Lett.* **77** 3865
[32] Blöchl P E 1994 *Phys. Rev. B* **50** 17953
[33] Kresse G and Joubert D 1999 *Phys. Rev. B* **59** 1758
[34] Kresse G and Furthmüller J 1996 *Comput. Mater. Sci.* **6** 15
[35] Kresse G and Furthmüller J 1996 *Phys. Rev. B* **54** 11169
[36] Grimme S, Antony J, Ehrlich S, and Krieg H 2010 *J. Chem. Phys.* **132** 154104
[37] Anisimov V I, Aryasetiawan F, and Lichtenstein A I 1997 *J. Phys.: Condens. Matter* **9** 767
[38] Yekta Y, Hadipour H, Şaşıoğlu E, Friedrich C, Jafari S A, Blügel S, and Mertig I 2021 *Phys. Rev. Mater.* **5** 034001
[39] Ji W, Lu Z Y, and Gao H J 2006 *Phys. Rev. Lett.* **97** 246101
[40] Köhler L and Kresse G 2004 *Phys. Rev. B* **70** 165405
[41] King-Smith R D and Vanderbilt D 1993 *Phys. Rev. B* **47** 1651
[42] Yang L, Gao Y X, Wu M H, and Jena P 2022 *Phys. Rev. B* **105** 094101
[43] Hu T and Kan E J 2019 *WIREs: Comput. Mol. Sci.* **9** e1409
[44] Guan Z, Hu H, Shen X W, Xiang P H, Zhong N, Chu J H, and Duan C G 2019 *Adv. Electron. Mater.* **6** 1900818